RESEARCH ARTICLE

Structural and Functional Insights into Peptidoglycan Access for the Lytic Amidase LytA of *Streptococcus pneumoniae*

Peter Mellroth,[a] Tatyana Sandalova,[b] Alexey Kikhney,[c] Francisco Vilaplana,[d] Dusan Hesek,[e] Mijoon Lee,[e] Shahriar Mobashery,[e] Staffan Normark,[a] Dmitri Svergun,[c] Birgitta Henriques-Normark,[a,f] Adnane Achour[b]

Department of Microbiology, Tumor and Cell Biology (MTC), Karolinska Institutet, Stockholm, Sweden[a]; Science for Life Laboratory, Center for Infectious Medicine (CIM), Department of Medicine, Karolinska University Hospital Huddinge, Karolinska Institutet, Stockholm, Sweden[b]; European Molecular Biology Laboratory (EMBL), Hamburg Outstation, Hamburg, Germany[c]; Division of Glycoscience, School of Biotechnology, Royal Institute of Technology (KTH), AlbaNova University Centre, Stockholm, Sweden[d]; Departments of Chemistry and Biochemistry, University of Notre Dame, Notre Dame, Indiana, USA[e]; Department of Laboratory Medicine, Division of Clinical Microbiology, Karolinska University Hospital, Stockholm, Sweden[f]

P.M. and T.S. contributed equally to this work.

ABSTRACT **The cytosolic *N*-acetylmuramoyl-L-alanine amidase LytA protein of *Streptococcus pneumoniae*, which is released by bacterial lysis, associates with the cell wall via its choline-binding motif. During exponential growth, LytA accesses its peptidoglycan substrate to cause lysis only when nascent peptidoglycan synthesis is stalled by nutrient starvation or β-lactam antibiotics. Here we present three-dimensional structures of LytA and establish the requirements for substrate binding and catalytic activity. The solution structure of the full-length LytA dimer reveals a peculiar fold, with the choline-binding domains forming a rigid V-shaped scaffold and the relatively more flexible amidase domains attached in a *trans* position. The 1.05-Å crystal structure of the amidase domain reveals a prominent Y-shaped binding crevice composed of three contiguous subregions, with a zinc-containing active site localized at the bottom of the branch point. Site-directed mutagenesis was employed to identify catalytic residues and to investigate the relative impact of potential substrate-interacting residues lining the binding crevice for the lytic activity of LytA. *In vitro* activity assays using defined muropeptide substrates reveal that LytA utilizes a large substrate recognition interface and requires large muropeptide substrates with several connected saccharides that interact with all subregions of the binding crevice for catalysis. We hypothesize that the substrate requirements restrict LytA to the sites on the cell wall where nascent peptidoglycan synthesis occurs.**

IMPORTANCE ***Streptococcus pneumoniae* is a human respiratory tract pathogen responsible for millions of deaths annually. Its major pneumococcal autolysin, LytA, is required for autolysis and fratricidal lysis and functions as a virulence factor that facilitates the spread of toxins and factors involved in immune evasion. LytA is also activated by penicillin and vancomycin and is responsible for the lysis induced by these antibiotics. The factors that regulate the lytic activity of LytA are unclear, but it was recently demonstrated that control is at the level of substrate recognition and that LytA required access to the nascent peptidoglycan. The present study was undertaken to structurally and functionally investigate LytA and its substrate-interacting interface and to determine the requirements for substrate recognition and catalysis. Our results reveal that the amidase domain comprises a complex substrate-binding crevice and needs to interact with a large-motif epitope of peptidoglycan for catalysis.**

Received 30 December 2013 **Accepted** 31 December 2013 **Published** 11 February 2014

Citation Mellroth P, Sandalova T, Kikhney A, Vilaplana F, Hesek D, Lee M, Mobashery S, Normark S, Svergun D, Henriques-Normark B, Achour A. 2014. Structural and functional insights into peptidoglycan access for the lytic amidase LytA of *Streptococcus pneumoniae*. mBio 5(1):e01120-13. doi:10.1128/mBio.01120-13.

Editor Rino Rappuoli, Novartis Vaccines and Diagnostics

Address correspondence to Adnane Achour, adnane.achour@ki.se.

Autolysins are bacterial cell wall hydrolytic enzymes that mediate antibiotic-induced lysis and may function as important virulence factors for bacterial pathogens. However, the molecular determinants that regulate the on and off modes of their lytic activities remain unclear. For antibiotics such as beta-lactams and vancomycin, the primary target is the cell wall synthesis machinery, which they stall either by binding irreversibly to the active site of penicillin-binding proteins (PBPs) or by forming an inhibitory complex with the muropeptide substrate utilized by PBPs. However, the consensus and molecular mechanisms that explain how blocking of cell wall synthesis leads to induction of autolysins are still not understood (1).

The major autolysin of *Streptococcus pneumoniae*, LytA, is unusual among bacterial autolysins in that it is produced in the bacterial cytosol and yet is an essential contributing factor for the organism to cause diseases, such as pneumonia, sepsis, and meningitis (2, 3). Although the mechanisms underlying LytA-mediated virulence remain unclear, bacterial expression of LytA and an autolytic behavior prevent phagocytosis and the production of phagocyte-activating cytokines (4). However, LytA appears not to be involved in cell wall processing or cell division during normal growth since *lytA*-deficient strains have growth rates similar to those of wild-type strains and display the same cell morphological phenotype (5). Recently, we investigated the func-

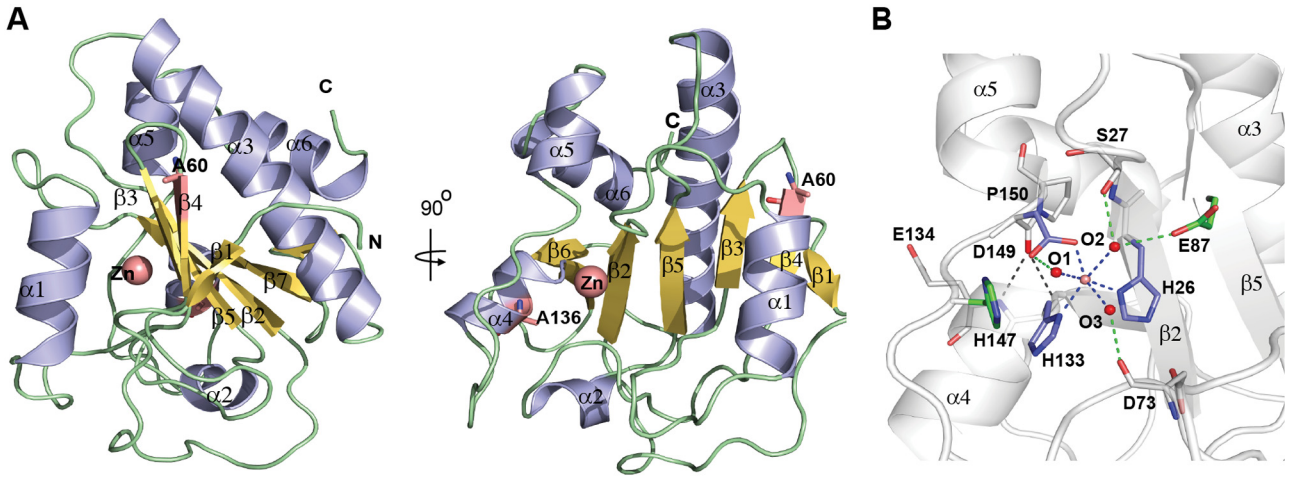

FIG 1 The catalytic N-terminal amidase domain of LytA contains a Y-shaped substrate-binding crevice. (A) The overall three-dimensional structure of LytA^{AMI} is presented in two perpendicular views. The catalytic Zn^{2+} ion is displayed as a pink sphere. The cysteine residues, both mutated to alanine, are also pink. α-Helices, β-sheets, and loops are colored purple, yellow, and green, respectively. (B) Interactions between the octahedrally coordinated Zn^{2+} ion and residues His26, His133, Asp149, and three water molecules within the active site are indicated by dashed purple lines. Catalytic residues, Zn^{2+} ligands, and residues coordinating water molecules are green, purple, and white, respectively. Two hydrogen bonds formed between *cis*-Pro150 and residues His133 and Glu134, both located on helix α4, are dashed gray lines. Hydrogen bonds formed between Zn^{2+}-bound water molecules and LytA^{AMI} residues are dashed green lines.

tional properties that are required for the induction of the bacteriolytic activity of LytA during growth, in stationary phase and following challenge with antibiotics (6). We found that lysis was not a consequence of a balanced competition between cell wall synthesis and cell wall degradation but instead that LytA was controlled at the level of substrate recognition and that the preferred substrate became available only when cell wall synthesis was interrupted. Thus, since pneumococci are insensitive for LytA-mediated lysis during exponential growth and get a LytA-sensitive phenotype during stationary phase or when cell wall synthesis is interrupted by antibiotic treatment or nutrient depletion, gross peptidoglycan (PG) might be capped to prevent spontaneous lysis (6).

In the present study, we have taken a structural and biochemical approach to investigate the mode by which LytA interacts with the peptidoglycan substrate. Our data demonstrate that LytA has a complex Y-shaped binding crevice with a substrate-interacting interface much larger than what has previously been reported for any related amidase. Mutagenic analysis and biochemical substrate interaction data suggest that for catalytic activity, LytA accepts only large-motif peptidoglycan epitope substrates containing several connected saccharides.

RESULTS

The N-terminal LytA domain adopts an amidase fold, and the active site contains an octahedrally coordinated zinc ion. The crystal structure of the N-terminal amidase domain of LytA (LytA^{AMI}) was refined to a 1.05-Å resolution, and the overall quality of the electron density was excellent, allowing for unequivocal positioning of all 172 residues comprised within the final three-dimensional model (Fig. 1A and Table 1). The LytA^{AMI} domain adopted an *N*-acetylmuramoyl-L-alanine amidase-like fold with a central β-sheet of seven strands and six flanking α-helices, all together forming an elliptical globular domain (Fig. 1A). A Zn^{2+} ion is coordinated octahedrally by the nitrogen atoms of histidine residues His26 and His133 (both 2.2 Å from Zn^{2+}), the OD_2 atom of the aspartate residue at position 149 (2.15 Å), and three water molecules (O_1, O_2, and O_3), all positioned 2.5 Å from Zn^{2+} (Fig. 1B). The Zn^{2+} ion combines with residues Glu87 and His147 in the catalytic site of LytA^{AMI}, localized on one side of the protein domain opposite the N and C termini (Fig. 1A and B). The three Zn^{2+}-coordinating residues His26, His133, and Asp149 are located on β-strand β2, at helix α4, and at the beginning of helix α5, respectively (Fig. 1B and Fig. S1 in the supplemental material). A *cis*-peptide bond formed between residues Asp149 and Pro150 in LytA^{AMI}, conserved among all known amidase_2 structures (Pfam01510), causes an adequate arrangement of helices α4 and α5 and is required for the structural positioning of the Zn^{2+}-binding residues His133 and Asp149 (Fig. 1A and B). Zinc ions usually involve tetrahedral or pentagonal coordination geometries in proteins, and only about 5% of all Zn^{2+} sites contain six ligands; LytA is to our knowledge the first example of an amidase with an octahedrally coordinated Zn^{2+} ion (7–9). The active-site residues in the catalytic center are fully conserved between LytA and the staphylococcal amidase AmiE, and we believe that the catalytic mechanisms recently proposed for AmiE may also hold true for LytA, with residues Glu87 and His147 of LytA having roles similar to those of residues Glu119 and His177 in AmiE (9) (Fig. 1B and Fig. S1).

Gram-positive *Firmicutes* adapt to oxidative environments by favoring the exclusion of cysteine residues from extracellular proteins, unless they are required for activity (10). We therefore at first hypothesized that Cys60 and Cys136 either could act as catalytic residues or were possibly required for proper folding of LytA^{AMI}. However, functional analysis demonstrated that the enzymatic activities of LytA variants with single and double alanine mutations were equivalent to that of wild-type LytA (wt-LytA) (Table 2). Furthermore, similar circular-dichroism (CD) spectra for mutated and wt-LytA indicated that replacement of both cysteine residues with alanine did not alter the folds of the LytA variants compared to that of wt-LytA (Fig. S2). Since residues Cys60 and Cys136 in wt-LytA are positioned 26 Å apart, the possibility of

TABLE 1 Data collection and refinement statistics

Parameter	Result(s) for[c]:		
	$LytA^{AMI}$	$LytA^{AMI}$	p-$LytA^{CBD}$
PDB code	4IVV		4IWT
Data collection statistics			
Wavelength (Å)	0.979	1.28 (Zn peak)	0.976
Resolution (Å) (range)	43.7–1.05 (1.11–1.05)	43.7–1.5 (1.58–1.5)	40.5–2.6 (2.74–2.6)
Space group	$P3_2$	$P3_2$	$P2_1$
Cell dimensions for *a*, *b*, *c* (Å)	50.4, 50.4, 72.6	50.4, 50.4, 72.5	40.58, 113.4, 40.64
α, β, γ (°)	90.0, 90.0, 120.0	90.0, 90.0, 120.0	90.0, 94.9, 90.0
No. of reflections[a]			
Observed	253,820 (36,305)	325,209 (44,377)	29,567 (3,739)
Unique	95,581 (14,111)	10,591 (4)	10,591 (1,495)
$<I/s(I)>$	7.3 (1.7)	30.0 (17.7)	7.4 (1.8)
Completeness (%)	99 (100)	99.9 (99.9)	93.9 (90.1)
R_{merge} (%)	6.8 (53.2)	5.7 (9.7)	14.0 (61.5)
Solvent content in the crystal (%)	53	53	52
B-factor from Wilson plot (Å^2)	8	12.8	48.5
Anomalous completeness (%)		99.7 (99.9)	
DelAnom correlation between half-sets		0.23 (0.3)	
Midslope of anomalous normal probability		1.554	
Refinement statistics[b]			
R_{cryst} (%)	14.97		21.16
R_{free} (%)	16.24		28.2
No. of atoms			
Total	1,640		2,509
Protein	1,427		2,478
Solvent	255		40
No. of ligands	2		10
Avg B-factor values			
Protein main chains (Å^2)	10.5		30.7
Protein side chains (Å^2)	12.3		31.7
Zn/choline (Å^2)	10		50
Solvent (Å^2)	31.2		25
RMSD from ideal geometry			
Bond length (Å)	0.006		0.01
Bond angle (°)	1.17		1.25
Ramachandran plot			
% of residues in preferred regions	98.7		94.4
% of residues in disallowed regions	0		0

[a] Values in parentheses correspond to the highest-resolution shell.
[b] Five percent of reflections were used for monitoring the refinement.
[c] The two colums for $LytA^{AMI}$ represent data sets collected at different X-ray wavelengths. Both sets were required for solving the structure.

a disulfide bond between the cysteine residues is also excluded (Fig. 1A).

LytA comprises a large Y-shaped substrate-binding crevice, and mutations in all three contiguous subregions negatively impact lytic activity. The structure of $LytA^{AMI}$ comprises an extended, wide, Y-shaped binding crevice, with the zinc-containing active site centrally located at the branch point between three contiguous subregions, designed α, β, and γ (Fig. 2A). Site-directed mutagenesis was performed in order to identify key substrate-binding and catalytic residues, and the lytic activity of each mutated LytA variant was compared to that of wt-LytA in a turbidometric lysis assay using pneumococcal cells as the substrate (Fig. 2A; Table 2). Alanine substitution of the catalytic residues His26, Glu87, His133, His147, and Asp149 and of the centrally localized residues His24, His54, and Lys131 abolished or significantly impaired LytA activity (Table 2; see also Fig. S3 in the supplemental material). Residues His24, His54, and Lys131 are not directly involved in catalysis but are buried and appear essential for the structural integrity of the active site. Mutation of several residues localized peripherally outside the LytA crevice did not have any negative effect on amidase activity (Table 2). However, replacement of residue Trp72, Gly75, or Asn79 with alanine reduced significantly LytA's amidase activity, demonstrating the importance of these three contiguous residues localized in the stem peptide-binding γ region. Importantly, mutations of the predicted peptidoglycan-interacting residues Gly29 and Val148 within the α region and Asn30, Ser33, Tyr41, and Arg44 of the β region all impaired the lytic activity of LytA, suggesting that multiple glycan interactions are required for efficient substrate binding (Fig. 2A and Table 2; see also Fig. S3).

The crystal structures of peptidoglycan recognition protein Iα (PGRP-Iα) and PGRP-Iβ have previously been determined in

TABLE 2 Activities of LytA point mutants in the turbidity lysis assay

Mutation(s)	Activity[a]	Function or position[b]
None (wt-LytA)	*****	
H24A	−	Buried
H26A	−	Zinc ligand
H54A	−	Buried
E87A	−	Catalytic
H133A	−	Zinc ligand
D149A	−	Zinc ligand
S33Q	*	β-Region
Y41A/R	*	β-Region
K131A	*	Buried
H147A/K	*	Catalytic
N30L/Q	***	β-Region
R44E/Q	***	β-Region
W72A	***	γ-Region
G75A	***	γ-Region
N79A	***	γ-Region
V148E/K	***	α-Region
G29A	****	α-Region
S33A	****	β-Region
C60R	****	Peripheral
S91A	****	Peripheral
K45R	*****	Branch point
F52A/V	*****	β-Region
C60A/E	*****	Peripheral
C60A + C136A	*****	Peripheral + buried
C136A	*****	Buried
T137A	*****	Peripheral
N142A	*****	Peripheral
H144A	*****	γ-Region
S145A	*****	Branch point
H166A	*****	Peripheral

[a] The relative enzymatic activities of LytA protein variants are given in the following intervals: *****, 100 to 80%; ****, 79 to 60%; ***, 59 to 40%; **, 39 to 20%; *, 19 to 5%; −, 4 to 0%.

[b] Buried residues are part of the hydrophobic core, and peripheral residues are surface-exposed residues outside the binding crevice. Zinc ligand and catalytic residues form the catalytic center. Branch point residues and α-, β-, and γ-regions represent subregions of the binding crevice.

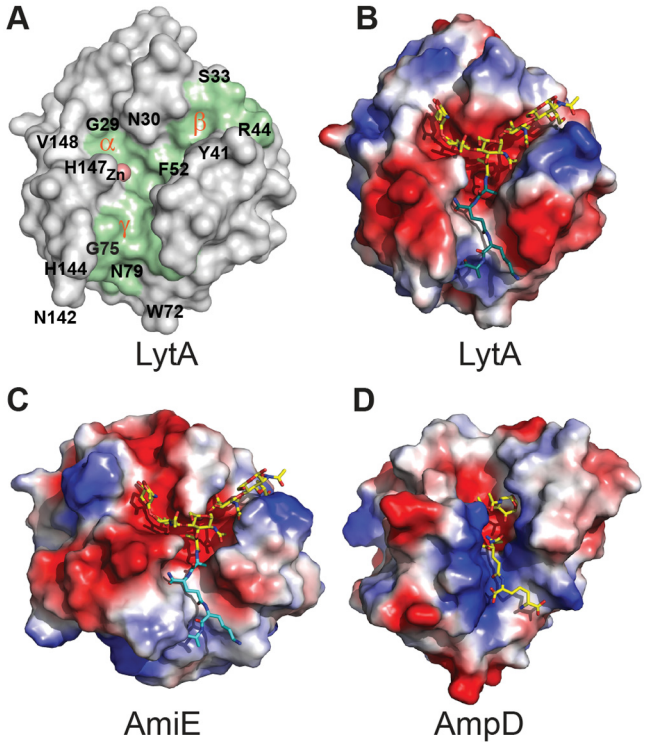

FIG 2 A muropeptide fragment comprising a pentasaccharide motif fits snugly within the Y-shaped substrate-binding crevice of LytA^{AMI}. (A) Surface of LytA^{AMI}, with the Y-shaped substrate-binding crevice colored in green and the three contiguous subregions α, β, and γ indicated. The catalytic Zn^{2+} ion is displayed as a pink sphere, and the locations of key substrate-interacting residues are marked. (B) A molecular model of a PG fragment consisting of five sugars (MurNAc-GlcNAc-MurNAc-GlcNAc-MurNAc, with a stem peptide linked to the central MurNAc) was placed within the substrate-binding crevices of LytA^{AMI}. The position of the substrate fragment M5P within the active site was first obtained by superposing the crystal structure of LytA^{AMI} on PGRP-Iα in complex with M5P (Protein Data Bank [PDB] accession number 2APH). Sugar chains and peptide stems were thereafter added to both ends of M5P in order to create the M(GM5P) GM fragment. The surface is colored according to electrostatic potentials; purple represents acidic and red basic residues. (C) The PG motif M(GM5P) GM fits snugly into the binding crevice of AmiE, taking the same conformation as in the molecular model of LytA. (D) The surface representation of the crystal structure of AmpD in complex with the reaction product reveals significant differences in the structural shapes and the electrostatic potentials of the substrate-binding crevice.

complex with muramyl penta- and tripeptides (M5P and M3P), respectively, and the *Citrobacter freundii*-derived cytoplasmic amidase AmpD has also been determined to be in complex with reaction products (29, 30, 31). Superimposition of these three amidase-ligand complexes on LytA^{AMI} indicated that a peptide stem linked to four to five saccharides would fit snugly into the Y-shaped binding groove of LytA^{AMI} (Fig. 2B). Interestingly, a similar peptidoglycan motif could also be fitted into the binding crevice of the staphylococcal amidase AmiE in ways nearly identical to those used in LytA, suggesting that a large substrate-interacting framework is important also for this enzyme (9) (Fig. 2C). A search for structural homologs to LytA^{AMI} using DALI (7) revealed that AmiE has the most similar structure, with a *Z* score of 21 (Table S1). Despite the fact that LytA^{AMI} has only 20% amino acid sequence identity to AmiE, the overall fold of LytA^{AMI} is rather similar to that of AmiE, with a root-mean-square deviation (RMSD) of 1.7 Å, following superimposition of the C-α atoms of 165 residues (Fig. S1 and Table S1). Almost all of the conserved residues either are catalytic or line the binding crevice. Importantly, most predicted substrate-interacting residues within the β-region of LytA are also conserved in AmiE, further implying that this subregion is also of importance for AmiE and that these enzymes may interact with the substrate in similar ways (Fig. S1 and Table S1). However, residues within the α-region display lower degrees of conservation, suggesting that minor differences in substrate preferences may exist (Fig. S1 and Table S1).

The second- and third-closest structural homologs to LytA, both with a *Z* score of 18, corresponded to the prophage-encoded endolysins PlyL and XlyA from *Bacillus anthracis* and *Bacillus subtilis*, respectively, with 21 to 22% sequence identity to LytA^{AMI} (Table S1) (34, 35). Superimposition of these two amidases onto LytA^{AMI} resulted in RMSD values of about 2 Å for 145 residues. PGRP-Iα and the amidase from *Citrobacter freundii*, AmpD, superposed onto LytA^{AMI} with *Z* scores of 12 to 14, confirming similar folds (29, 31). However, both the *Escherichia coli*-associated amidase AmiD (32) and the *Listeria monocytogenes* phage endolysin amidase PSA (33) displayed lower *Z* scores of 11 and 8.5, respectively. Thus, despite significant overall fold similarity, pro-

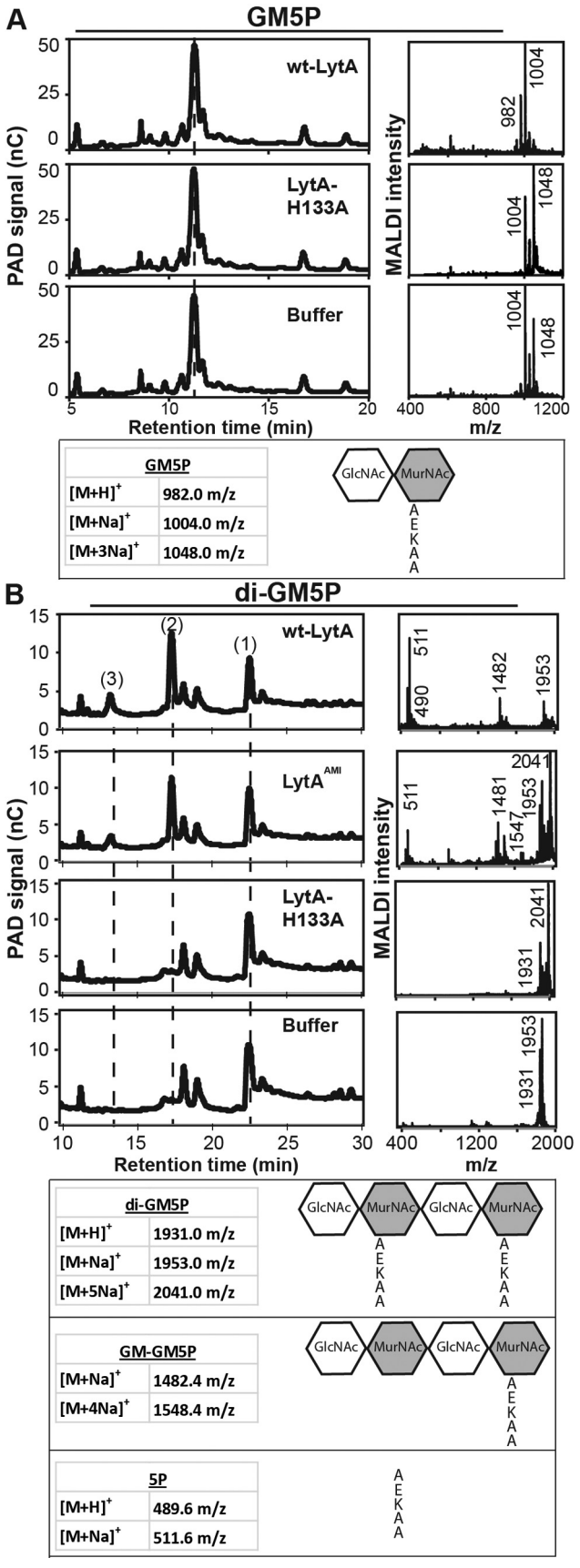

teins that belong to the amidase_2 family share only 10 to 20% sequence identity, including often only residues essential for catalytic activity and Zn^{2+} binding (Table S1).

The bacillus-specific PlyL and XlyA amidases also share conserved residues within the β-region, indicating that a Y-shaped binding crevice may be a common feature for Gram-positive amidases (Table S1). In contrast, the binding groove of AmpD lacks the β-region altogether, which may reflect a functional adaptation to peptidoglycan recycling and catalysis of muropeptides with only one or two saccharide moieties (29) (Fig. 2D). In conclusion, LytA contains a Y-shaped binding crevice that can accommodate a muropeptide substrate allowing for extensive interactions with glycan residues localized on both sides of the central MurNAc.

Multiple interactions between the substrate and LytA are required for efficient binding and cleavage. Since the structure of the substrate interface indicated that a peptidoglycan fragment with a large glycan portion could fit into the binding crevice (Fig. 2B), we investigated the activity of LytA against defined muropeptides with one saccharide linked to a pentapeptide (MurNAc-L-Ala-iso-D-Glu-L-Lys-D-Ala-D-Ala) (M5P); two saccharides linked to a pentapeptide (GlcNAc-MurNac-L-Ala-iso-D-Glu-L-Lys-D-Ala-D-Ala) (GM5P); or four connected saccharides with pentapeptides linked via the MurNAc residues (GlcNAc-MurNac-GlcNAc-MurNAc-(2x)-L-Ala-iso-D-Glu-L-Lys-D-Ala-D-Ala) (di-GM5P). Our data suggest that neither M5P nor GM5P was processed following a 24-h incubation with full-length LytA (Fig. 3A and S4), which stands in contrast to what has previously been reported for AmiE (9) and possibly indicates differences in substrate specificity between LytA and AmiE. However, following incubation of wt-LytA or $LytA^{AMI}$ with di-GM5P, new product peaks were recorded by high-pH anion-exchange chromatography coupled with pulsed amperometric detection (HPAEC-PAD) chromatograms (Fig. 3B). The new product peaks were unequivocally assigned to GM-GM5P and pentapeptide 5P fragments using matrix-assisted laser desorption ionization–time of flight mass spectrometry (MALDI-TOF MS), which clearly indicates that the presence of at least one *N*-acetylglucosamine moiety on each side of M5P is required for efficient cleavage by LytA (Fig. 3B). The fact that no cleavage was recorded with the GM5P substrate, which would interact with the α- and γ-regions of the binding crevice, strongly indicates that additional interactions within the β-region are required for catalysis. It should also be noted that the cleavage efficiencies of both full-length LytA and truncated $LytA^{AMI}$ were low, as a substantial portion of the substrate remained uncleaved after 48 h of incubation of PG derivatives with LytA, emphasizing

FIG 3 A motif corresponding to the tetrasaccharide muropeptide substrate (di-GM5P) is cleaved by LytA. (A) Incubation of the GM5P substrate with LytA or inactive LytA-H133A does not result in any product peak, as demonstrated by the HPAEC-PAD analysis. The chromatogram for GM5P incubated in buffer alone is provided for comparison. The masses of the substrate peak were determined using MALDI-TOF MS (right panels). Calculated masses and a cartoon of the corresponding substrate are shown (lower panels). (B) Incubation of the tetra-saccharide substrate di-GM5P (peak 1) with either wt-LytA or Lyt^{AMI} resulted in the production of two new peaks (2 and 3), as determined by HPAEC-PAD. In contrast, no peaks appeared following incubation with inactive LytA-H133A. The profile of di-GM5P incubated with buffer alone is also provided as a reference. The masses of the substrate and of each product peak were determined using MALDI-TOF MS (right panels). Calculated masses of the substrate (di-GM5P) and products (GMGM5P and 5P) and corresponding cartoons are shown (lower panels).

that the substrate might not be fully optimal (Fig. 3). No cleaved products were detected following incubation with the inactive LytA-H133A control variant, devoid of a zinc ligand histidine (Fig. 3A and B).

Microscale thermophoresis was used to determine the binding affinities of LytA toward the muropeptides M5P, GM5P, and di-GM5P, employing enzymatically inactive LytA-H133A, which can bind but not cleave the substrates. Our data revealed that the tetrasaccharide muropeptide di-GM5P bound to LytA-H133A with a 2- to 3-fold-higher affinity than the disaccharide muropeptide GM5P and with a 20-fold-higher affinity than M5P. Average dissociation constant (K_d) values of 50 ± 13 and 120 ± 17 μM were calculated for di-GM5P and GM5P, respectively, out of three independent experiments. For M5P, we did not obtain a proper curve with up to 1 mM of substrate, suggesting that the K_d is more than 800 μM (Fig. S5).

The full-length CBD of prophage LytA comprises six choline-binding sites. The crystal structure of the full-length choline-binding domain (CBD) (residues 173 to 318) from prophage LytA (p-LytA^{CBD}) was determined to a 2.6-Å resolution in the presence of choline (Fig. 4A). This structure, which together with the presented amidase domain comprises the entire LytA protein, is larger than the truncated forms of the CBD of LytA, which has previously been reported (13, 14). However, as expected from the 93% sequence identity and 97% similarity between endogenous and prophage CBDs (Fig. S1), p-LytA^{CBD} displayed a solenoid fold similar to a 76-Å-long crooked cylinder with a 21-Å radius (14). The overall structure of p-LytA^{CBD} was similar to that of endogenous LytA^{CBD}, with RMSD values of 0.78, 1.01, and 1.38 Å following superimposition of p-LytA^{CBD} on previously published LytA^{CBD} structures with PDB codes 1GVM (13), 1HCX (14), and 2BML (15), respectively. The first β-hairpin (residues 177 to 189) of p-LytA^{CBD}, not present in previously published crystal structures of LytA^{CBD}, takes a typical superhelical fold (Fig. 4A) (13, 14). Though this first choline-binding repeat differs both sequentially (10 to 25% identity) and structurally (RMSD values ranging from 1.3 to 2.3 Å) from the five other choline-binding repeats, an additional choline-binding site, localized between hairpins β8/β9 and β10/β11, comprised all elements necessary for choline binding, including a tryptophan residue at the third position of the β8 strand, three aromatic residues within the β9 strand, and a glycine residue at position 3 of the turn, which links the first choline-binding repeat to the next repeat (Fig. S1 and 4B). However, while clear electron density for choline was found in each of the other repeats, no electron density corresponding to a choline molecule was found in the first conventional binding site localized between residues Trp178 and Tyr185 (Fig. 4B). This may be due to crystal packing, since the side chain of residue Lys265 in another closely positioned CBD subunit within the asymmetric unit could dislodge the choline molecule. Instead, an unequivocal electron density peak for a choline moiety was identified between Trp186 on strand β9 and Tyr194, localized on the loop that links β9 and β10 (Fig. 4B). Thus, full-length p-LytA^{CBD} contains six choline-binding sites. Finally and as with endogenous LytA^{CBD}, the last hairpin formed by strands β20 and β21 (residues 305 to 318) in p-LytA^{CBD} is not involved in choline binding and is instead important for dimerization (11).

The dimerization mode of p-LytA^{CBD} was similar to that of previously determined crystal structures of endogenous LytA^{CBD} (13, 14). Each p-LytA^{CBD} formed a V-shaped dimer with its symmetry-related counterpart, with a buried surface area of 960 Å^2, through stacking of the β20/β21 hairpin from each monomer (Fig. 4C). A total of six hydrogen bonds tightened the interactions between the two subunits of the p-LytA^{CBD} dimer, with an angle of about 90° formed between the axis of the two subunits,separating the first two choline molecules (CholA1 and CholB1) by 63 Å (Fig. 4C). Superimposition of the p-LytA^{CBD} dimer on the endogenous LytA^{CBD} dimer resulted in an RMSD value of 1.4 Å for 256 aligned C-α atoms, indicating identical dimerization modes.

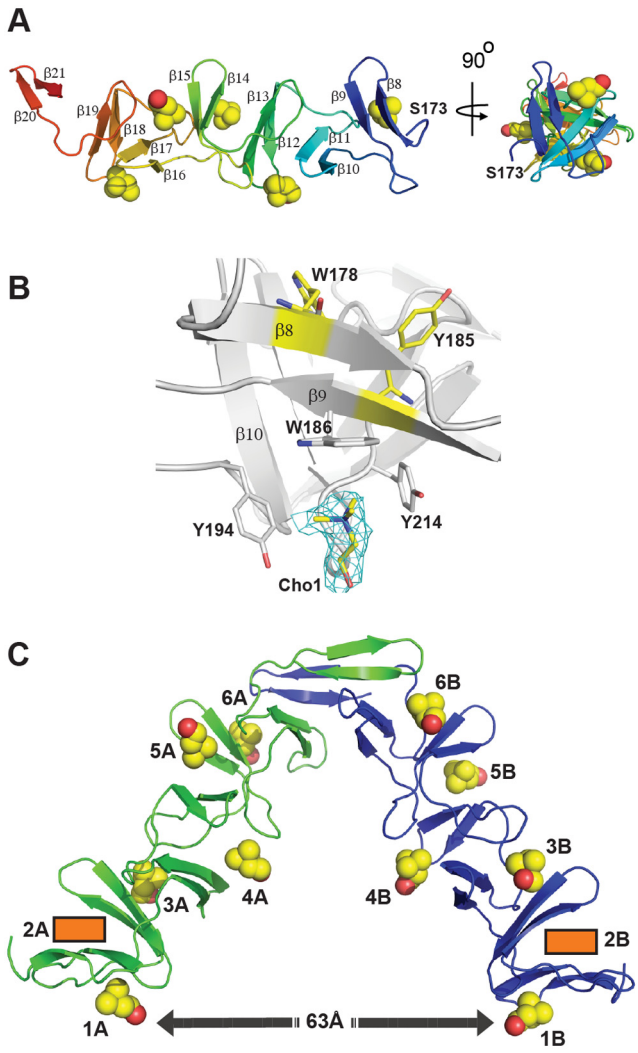

FIG 4 The C-terminal domain of phage LytA contains six choline-binding sites. (A) Two perpendicular views of the crystal structure of p-LytA^{CBD}, comprising residues 173 to 318. The numbering of the β-strands, starting with number 8, reflects their positions in the full-length LytA (numbers 1 to 7 in the amidase domain). The β-hairpin formed by β8 and β9 constitute the last-step, solenoid-shaped choline-binding domain, which faces the amidase domain on its N-terminal side. (B) The classical choline-binding site, localized between residues Trp178 and Tyr185, was not occupied by a choline molecule in the crystal, most likely due to a crystal packing artifact. However, a clear electron density for choline was present in the second nonclassical choline-binding site formed by residues Trp186, Tyr194, and Tyr214. The 1σ electron density in the $2F_o$-F_c omit map is displayed in blue. (C) The dimer of p-LytA^{CBD}, generated along the crystallographic 2-fold axis, indicates the possibility for simultaneous binding of 12 choline molecules. Orange boxes represent consensus choline binding sites that were not occupied by cholines in the crystal structure.

The full-length LytA dimer adopts a V-shaped rigid scaffold formed by two choline-binding domains with flexible amidase domains attached in a *trans* conformation. The oligomeric states and the conformations adopted by LytA were analyzed using small-angle X-ray scattering (SAXS). The scattering profiles of full-length wt-LytA and phage LytA were almost identical (Fig. 5A). A molecular mass of 75 ± 8 kDa, derived from the Guinier approximation, corresponded to those of dimeric proteins. Furthermore, the radius of gyration (R_g) and the maximum dimension (D_{max}) were 49 ±5 Å and 150 ±15 Å, respectively, indicating a rather extended structure of the dimers.

Recombinant full-length His-tagged LytA that had been purified and stored in buffers without choline appeared as a monomer in solution, with a molecular mass and R_g of 40 ±4 kDa and 34 ±3 Å, respectively. It formed a dimer when 5 mM choline chloride was added to the same batch of protein, confirming that dimerization of wt-LytA directly depends on the presence of choline chloride (11) (Fig. 5A and Table S2). Furthermore, SAXS analysis of monomeric and dimeric LytAs did not reveal any major conformational changes upon dimerization, suggesting that C-terminal choline-binding domains do not affect amidase activity through sterical hindrance of the active site or through other conformational alterations (Fig. 5A). The choline-binding domains formed dimers in solution also in the absence of the amidase domains, and these dimers were very similar to those found in all crystal structures of CBDs, including the one presented in this study (Fig. 5A). The conformation and dimerization modes of amidase-free CBD dimers, as in $LytA^{CBD}$, also superimposed very well on full-length LytA dimers, suggesting that the amidase domains do not affect the conformation of the CDB dimer.

The *ab initio* shape of the full-length LytA clearly displayed a $LytA^{CBD}$ dimer attached to two amidase domains (Fig. 5B). A hybrid model, constructed using the crystal structures of $LytA^{AMI}$ (residues 1 to 172) and of the p-$LytA^{CBD}$ dimer (residues 173 to 318) (Fig. 5C) and performed using P2 symmetry, fitted well to the SAXS experimental data ($\chi = 1.5$) (Fig. 5A) (see Text S1 for the definition of chi). The two structures were moved and rotated as rigid bodies, whereas the linker (residues 171 to 175) between $LytA^{AMI}$ and $LytA^{CBD}$ was represented as a chain of dummy residues. The hybrid model agrees very well with the *ab initio* model (Fig. 5B) and reveals that the amidase domains are positioned in *trans* relatively to the plane formed by the C-terminally linked V-shaped CBDs (Fig. 5C). Thus, direct interaction between the amidase domains is not possible, since the minimal distance between the zinc atoms in each active site is 120 Å. While our SAXS results demonstrated that the CBD dimer remained rigid, ensemble optimized method (EOM) (12) analysis of a pool of 10,000 randomly generated models revealed a certain level of lateral flexibility for the two $LytA^{AMI}$ domains (Fig. S6). In conclusion, our SAXS analysis of LytA shows that two choline-binding domains form a rigid V-shaped scaffold and that the amidase head groups are attached in the *trans* position. Thus, in the pneumococcal cell wall, the LytA dimer associates with teichoic acids by affinity binding to several choline residues, and the flexible amidase domains can likely adjust their orientation for proper binding to the nascent peptidoglycan.

DISCUSSION

The present study combines structural and biochemical data to investigate how the major pneumococcal autolysin LytA interacts with the peptidoglycan substrate. The 1.05-Å structure of the amidase domain of LytA reveals a wide Y-shaped binding crevice with a catalytic zinc-containing center located at the bottom of the branch point. Mutational analysis suggested that residues lining all subregions of binding crevices impact amidase activity and that a large-motif muropeptide substrate with four connected saccharides is required for enzymatic catalysis. However, incomplete substrate catalysis and substrate-binding affinity in the micromolar range indicate that even if di-GM5P is a possible substrate, it might be a suboptimal one. Comparative analysis suggested that the staphylococcal amidase AmiE may have a larger substrate interface than what has previously been reported (9). Indeed, LytA and AmiE appear to share a Y-shaped binding crevice with similar electropotential surface distributions as well as the conservation of substrate-binding residues, which strongly indicates similar substrate recognition interfaces (Fig. 2B and C). However, in contrast to LytA, AmiE displays activity toward M5P and GM5P, which might be explained by the lower conservation of residues within the α-region (9) (Fig. S1 and Table S1). Interestingly, AmiE is actively secreted into the extracellular cell wall environment, whereas LytA, which lacks an N-terminal signal peptide, is constitutively expressed and resides mainly in the cytoplasm (3, 6, 9). Thus, the inability of LytA to cleave small muropeptides may be a functional adaptation, since the synthesis of peptidoglycan precursors resulting in the formation of lipid II is encompassed within a disaccharide structural framework and also takes place in the cytosol, which could otherwise interfere with cell wall synthesis and cellular growth (6).

The presented structure of the choline-binding domain is similar to previously published structures but includes the entire domain and reveals an additional beta hairpin and in all six potential choline-binding sites (13, 14). The two crystal structures combined encompass the entire LytA protein, and with SAXS analysis, we could obtain a model for the full-length LytA protein. The peculiar structure of the LytA dimer with the rigid V-shaped scaffold formed by the choline-binding domains and the more flexible amidase domains in the *trans* position, as determined by the SAXS analysis, likely provide important information about how LytA interacts with the substrate or cell wall. Indeed, it has previously been shown that truncated LytA forms that lack the terminal beta hairpin cannot dimerize and have drastically reduced lytic activity, suggesting that the structure of the dimer revealed by the SAXS analysis is also functionally relevant (16). The ~120-Å distance between the two catalytic centers suggests that the amidase domains may interact with murein epitopes on different glycan strands. The large glycan interface within the binding crevice also opens up the possibility that cleavage may be sequential and directional along the glycan strands.

Initial attachment of LytA to teichoic acids via the choline-binding domain targets the protein to the equatorial region of the pneumococcal cell wall (6, 17, 18). A similar cell wall association was reported for AmiE, which was shown to bind specifically to lipid-anchored teichoic acids (LTA) (19, 20). However, in pneumococci, both the wall-associated teichoic acids (WTA) and LTA share the same phospho-glycan polymeric repeats, suggesting that LytA may not discriminate between them (21). Conversely, in contrast to LytA, the pneumococcal glucosaminidase LytB displays a polar association, suggesting a certain degree of specificity in cell wall targeting among different choline-binding proteins (17). Thus, equatorial positioning of the amidases brings them to

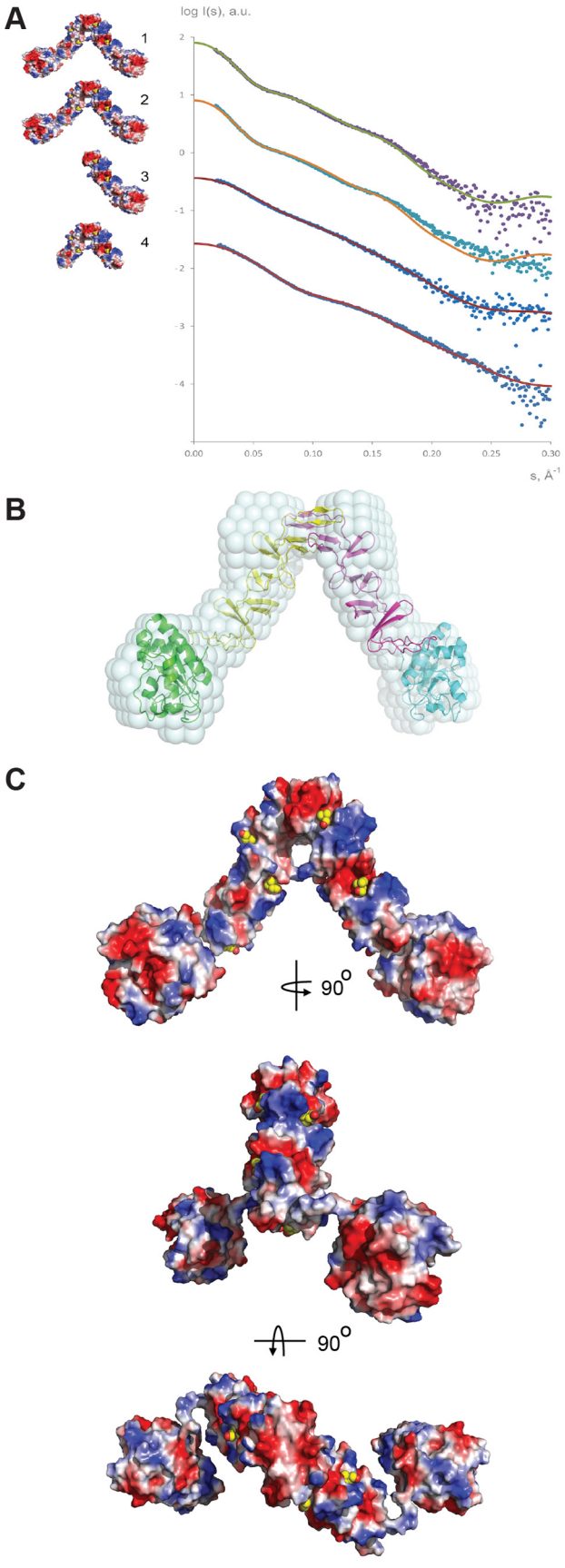

the region where nascent peptidoglycan is synthesized by the cell wall divisome and brings them proximal to regions where a putative substrate for LytA was observed in ~150-nm zones immediately adjacent to the pneumococcal equator (6). Since inhibition of cell wall synthesis, for example, by beta-lactams or vancomycin, is a prerequisite for the induction of LytA- and AmiE-mediated lysis, the PBP-containing, murein-synthesizing protein complexes may regulate the access of these amidases to their substrates (1, 6). This hypothesis was recently supported by the finding that PBP2b depletion induced a LytA-sensitive phenotype during exponential growth (22).

The data presented here reveal a complex Y-shaped binding crevice with an extensive substrate-interacting interface at which multiple residues in all three subregions are involved in substrate recognition and are required for efficient catalysis. Moreover, LytA discriminated among substrates and accepted only a large-motif peptidoglycan epitope with several connected saccharides to drive amidase activity. These data are well in line with the model suggesting that LytA is controlled at the level of substrate recognition and support the idea that the integrity of the polymerized peptidoglycan cell wall may include a molecular modification or structural determinant that is recognized in a key and keyhole relationship allowing for the substrate to be included or excluded from fitting into the binding crevice. However, at present, we are restricted from studying these issues in detail by the limited availability of defined, large-epitope muropeptide substrates and the complexity of the intact cell wall. Further studies are warranted to describe the nature of the LytA-protective factor present in the gross peptidoglycan and the enzyme(s) responsible for its incorporation.

MATERIALS AND METHODS

Cloning and mutagenesis of *S. pneumoniae*-associated and prophage-specific LytA. Cloning of the endogenous *lytA* from the *S. pneumoniae* TIGR4 strain in the expression vector pET21d has been described previously (6). The prophage-specific *lytA* (SPH_0121) from the Hungary 19A-6 strain (ATCC 700673) was amplified by PCR from chromosomal DNA with primers containing NheI and HindIII overhang sequences and ligated into the pET21d expression vector. All mutations in pET21d-*lytA* were introduced using the QuikChange II mutagenesis kit (Agilent Technologies) and oligonucleotide primers with a degenerate sequence at the site for the target codon. An N-terminal His_6 tag was introduced by adding six-histidine codons to mutagenic primers between the ATG start codon and the second codon. Similarly, C-terminal His_6-tagged truncation variants were created by adding six-histidine codons, followed by a stop codon on the primers at the mutation site.

FIG 5 The full-length LytA dimer adopts a rigid V-shaped scaffold with the two amidase domains in the *trans* configuration. (A) SAXS data demonstrate that the wild type and bacteriophage LytA are similar in shape and that both form dimers in solution in the presence of choline (curves 1 and 2, respectively). Without choline, the same molecule is monomeric in solution (curve 3). The CBD of wt-LytA forms a dimer in solution, in line with results from the crystal structure (curve 4). The logarithm of the scattering intensity is displayed versus momentum transfer ($s = 4\pi \sin\theta/\lambda$), where 2θ is the scattering angle and λ (the X-ray scattering wavelength) is 1.5 Å. The data for different samples were offset vertically for clarity (dots, experimental data; smooth curves, scattering computed from the models). a.u., arbitrary units. (B) *Ab initio* model of the wt-LytA dimer (gray spheres) superimposed with the best rigid-body model using the crystal structures of $LytA^{AMI}$ and p-$LytA^{CBD}$ (ribbons). (C) Three perpendicular views of the rigid-body model of the full-length LytA dimer reveal the *trans* configurations of the amidase domains. Surfaces are colored according to surface charge representation.

Recombinant protein expression and purification were performed as previously described (6).

Turbidometric amidase activity assay. Amidase activity was analyzed by measuring the decrease in turbidity of T4Δ*lytA* cells after challenge with recombinant LytA protein. T4Δ*lytA* cells, grown to early stationary phase in C+Y medium (36), were sedimented by centrifugation, washed twice with phosphate-buffered saline (PBS), resuspended in PBS with 5% glycerol, and thereafter kept frozen until use. To measure activity, thawed cells were distributed into wells of a multiwell plate to an optical density at 600 nm (OD_{600}) of 1.0 and incubated at 37°C in a Bioscreen reader (OY Growth Curves AB Ltd., Helsinki, Finland). The distributed cells were challenged with 10 μg/ml of wild-type and mutated recombinant LytA proteins, and the optical density (600 nm) was recorded at 10-min intervals. The initial rates of decrease in turbidity (ΔOD_{600}/min) were determined for each protein, and their relative activities were calculated in relation to that of wt-LytA using the average of results from three independent reactions.

Analysis of muropeptide digestion with HPAEC-PAD and MALDI-TOF MS. Muropeptides M5P, GM5P, and di-GM5P were synthesized as previously described (23, 24). The muropeptides (1 mM) were incubated with 10 μg/ml of wt-LytA, $LytA^{AMI}$, LytA-H133A, or no protein in PBS supplemented with 10 mM choline chloride. Incubations were performed with continuous shaking for 8 h at 37°C, followed by 40 h at 20°C. The synthetic muropeptide substrates and their degradation products after enzymatic incubations were analyzed by HPAEC-PAD using a Dionex 3000 system (Dionex, Sunnyvale, CA, USA) in a PA1 anion-exchange column at 1 ml/min. After equilibration in 100 mM NaOH, 10 μl of sample was injected and separation was carried out using the following gradient elution profile: (i) a linear gradient from 100 mM NaOH to 100 mM NaOH-200 mM sodium acetate (NaOAc) until 20 min, (ii) a linear gradient to 100 mM NaOH-800 mM NaOAc until 40 min, and (iii) isocratic elution at 100 mM NaOH-800 mM NaOAc until the final time of 45 min prior to reequilibration. The pulsed amperometric detector was configured using a typical carbohydrate program, with electrode potentials (E) set as follows: the first E (E_1) was 0.1 V, the E_2 was −2.0 V, the E_3 was 0.6 V, and the E_4 was −0.1 V. Corresponding applied durations (time [t]) were as follows: t_1 was 400 ms, t_2 was 30 ms, t_3 was 10 ms, and t_4 was 60 ms, respectively, with integration between 200 and 400 ms. The identification of substrates and products after enzymatic incubations was performed by MALDI-TOF MS using a LaserToF LT3 Plus instrument (SAI, Manchester, United Kingdom). Incubation mixtures were premixed with matrix solution (10 g/liter 2,5-dihydroxybenzoic acid [DHB] in 50% [vol/vol] acetone) in a 1:10 ratio and spotted directly onto a standard steel MALDI plate prior to analysis. Mass spectra were collected in the reflectron mode with both positive and negative ionization.

Crystallization of the amidase domain of LytA. All attempts to crystallize the wild type and several mutated versions of full-length LytA were unsuccessful. Similarly, we were unable to determine crystallization conditions for the amidase domain of wt-LytA (corresponding to residues 1 to 179). In contrast, crystals of the amidase domain of LytA, in which the two cysteine residues, Cys60 and Cys136, were changed to alanines, were obtained in hanging drops by vapor diffusion in 12% polyethylene glycol 6000, 0.8 M LiCl, 100 mM Tris-HCl, pH 6.7. Typically, 2 μl of a 5.2-mg/ml protein solution were equilibrated against a 2-μl reservoir solution at 20°C.

SAXS measurement and data analysis. Prior to SAXS measurements, the purified full-length LytA, prophage-LytA, and $LytA^{CBD}$ were dialyzed extensively against 20 mM Tris, pH 7.5, 150 mM NaCl, 5 mM choline chloride, 1 μM $ZnCl_2$. A batch of wt-LytA(N-His_6), purified on a Ni-nitrilotriacetic acid (NTA) column which had not been in contact with choline chloride, was split in two fractions. While the first fraction was dialyzed against 20 mM Tris, pH 7.5, 150 mM NaCl, 5 mM choline chloride, and 1 μM $ZnCl_2$, the second fraction was dialyzed against 20 mM Tris pH 7.5, 150 mM NaCl, 1 μM $ZnCl_2$.

Small-angle X-ray scattering data were collected from all protein solutions on the X33 camera at the EMBL on the DORIS III storage ring (DESY, Hamburg, Germany) (25). Using a photon-counting Pilatus 1M detector at a sample-detector distance of 2.7 m and a wavelength (λ) of 1.5 Å, the range of momentum transfer, $0.01 < s < 0.6$ Å^{-1}, was covered ($s = 4\pi \sin\theta/\lambda$, where 2θ is the scattering angle). For each construct, several solute concentrations ranging from 1 to 10 mg/ml were measured. Radiation damage was monitored by comparing eight successive 15-s exposures, and no significant changes were observed. Data were normalized to the intensity of the transmitted beam and radially averaged. The scattering of the buffer was subtracted, and the difference curves were scaled for protein concentration. The low-angle data were extrapolated to infinite dilution and merged with the higher-concentration high-angle data to yield the final composite scattering curves. The data-processing steps were performed using the automated SAXS data-processing pipeline (26).

The forward scattering, $I(0)$, and the radius of gyration, R_g, were evaluated using the Guinier approximation (27), with the assumption that, at very small angles ($s < 1.3/R_g$), the intensity is represented by $I(s) = I(0) \exp[-(sR_g)2/3]$. These parameters were also computed from entire scattering patterns using the indirect transform package GNOM (28), which provided the pair distribution function of the particle, $p(r)$, and the maximum dimension, D_{max}. The molecular mass of the solute was evaluated against the forward scattering from a reference bovine serum albumin solution (66 kDa). The excluded volumes of the hydrated particles were computed with AUTOPOROD (12). The volumes (Porod) in Å^3 are about 1.6 times the molecular masses in Da for globular proteins.

SUPPLEMENTAL MATERIAL

Supplemental material for this article may be found at http://mbio.asm.org/lookup/suppl/doi:10.1128/mBio.01120-13/-/DCSupplemental.

Text S1, PDF file, 0.1 MB.
Figure S1, TIF file, 12.9 MB.
Figure S2, TIF file, 4.6 MB.
Figure S3, TIF file, 3.1 MB.
Figure S4, TIF file, 11 MB.
Figure S5, TIF file, 6 MB.
Figure S6, TIF file, 9.7 MB.
Table S1, DOCX file, 0.1 MB.
Table S2, DOCX file, 0.1 MB.

ACKNOWLEDGMENTS

We gratefully acknowledge access to synchrotron beamline ID29 at ESRF (Grenoble, France) and the EMBL beamline at the DORIS III storage ring at DESY (Hamburg, Germany). We also thank the Protein Science Facility, Karolinska Institutet (http://psf.ki.se/), and the company NanoTemper Technologies GmbH for access to instruments.

This work was supported by grants from the Swedish Research Council (A.A., B.H.-N., S.N.), Swedish Foundation for Strategic Research (A.A., B.H.-N., S.N.), the Knut and Alice Wallenberg Foundation (A.A., B.H.-N., S.N., F.V.), the Wenner Gren Foundation (T.S.), the EU 7th Framework Programme (Infrastructures grant BioStruct-X; contract 283570) (D.S., A.K.), and the National Institutes of Health (S.M., D.H., M.L.).

REFERENCES

1. **Tomasz A, Waks S.** 1975. Mechanism of action of penicillin: triggering of the pneumococcal autolytic enzyme by inhibitors of cell wall synthesis. Proc. Natl. Acad. Sci. U. S. A. **72:**4162–4166. http://dx.doi.org/10.1073/pnas.72.10.4162.
2. **Hirst RA, Gosai B, Rutman A, Guerin CJ, Nicotera P, Andrew PW, O'Callaghan C.** 2008. Streptococcus pneumoniae deficient in pneumolysin or autolysin has reduced virulence in meningitis. J. Infect. Dis. **197:**744–751. http://dx.doi.org/10.1086/527322.
3. **Briese T, Hakenbeck R.** 1985. Interaction of the pneumococcal amidase with lipoteichoic acid and choline. Eur. J. Biochem. **146:**417–427. http://dx.doi.org/10.1111/j.1432-1033.1985.tb08668.x.
4. **Martner A, Skovbjerg S, Paton JC, Wold AE.** 2009. Streptococcus pneumoniae autolysis prevents phagocytosis and production of

phagocyte-activating cytokines. Infect. Immun. **77:**3826–3837. http://dx.doi.org/10.1128/IAI.00290-09.
5. **Tomasz A, Moreillon P, Pozzi G.** 1988. Insertional inactivation of the major autolysin gene of Streptococcus pneumoniae. J. Bacteriol. **170:**5931–5934.
6. **Mellroth P, Daniels R, Eberhardt A, Rönnlund D, Blom H, Widengren J, Normark S, Henriques-Normark B.** 2012. LytA, major autolysin of Streptococcus pneumoniae, requires access to nascent peptidoglycan. J. Biol. Chem. **287:**11018–11029. http://dx.doi.org/10.1074/jbc.M111.318584.
7. **Cheng X, Zhang X, Pflugrath JW, Studier FW.** 1994. The structure of bacteriophage T7 lysozyme, a zinc amidase and an inhibitor of T7 RNA polymerase. Proc. Natl. Acad. Sci. U. S. A. **91:**4034–4038. http://dx.doi.org/10.1073/pnas.91.9.4034.
8. **Harding MM.** 2001. Geometry of metal-ligand interactions in proteins. Acta Crystallogr. D Biol. Crystallogr. **57:**401–411. http://dx.doi.org/10.1107/S0907444900019168.
9. **Zoll S, Pätzold B, Schlag M, Götz F, Kalbacher H, Stehle T.** 2010. Structural basis of cell wall cleavage by a staphylococcal autolysin. PLoS Pathog. **6:**e1000807. http://dx.doi.org/10.1371/journal.ppat.1000807.
10. **Daniels R, Mellroth P, Bernsel A, Neiers F, Normark S, von Heijne G, Henriques-Normark B.** 2010. Disulfide bond formation and cysteine exclusion in gram-positive bacteria. J. Biol. Chem. **285:**3300–3309. http://dx.doi.org/10.1074/jbc.M109.081398.
11. **Romero P, López R, García E.** 2007. Key role of amino acid residues in the dimerization and catalytic activation of the autolysin LytA, an important virulence factor in Streptococcus pneumoniae. J. Biol. Chem. **282:**17729–17737. http://dx.doi.org/10.1074/jbc.M611795200.
12. **Petoukhov MV, Franke D, Shkumatov AV, Tria G, Kikhney AG, Gajda M, Gorba C, Mertens HDT, Konarev PV, Svergun DI.** 2012. New developments in the ATSAS program package for small-angle scattering data analysis. J. Appl. Crystallogr. **45:**342–350. http://dx.doi.org/10.1107/S0021889812007662.
13. **Fernández-Tornero C, García E, López R, Giménez-Gallego G, Romero A.** 2002. Two new crystal forms of the choline-binding domain of the major pneumococcal autolysin: insights into the dynamics of the active homodimer. J. Mol. Biol. **321:**163–173. http://dx.doi.org/10.1016/S0022-2836(02)00596-X.
14. **Fernández-Tornero C, López R, García E, Giménez-Gallego G, Romero A.** 2001. A novel solenoid fold in the cell wall anchoring domain of the pneumococcal virulence factor LytA. Nat. Struct. Biol. **8:**1020–1024. http://dx.doi.org/10.1038/nsb724.
15. **Fernández-Tornero C, García E, de Pascual-Teresa B, López R, Giménez-Gallego G, Romero A.** 2005. Ofloxacin-like antibiotics inhibit pneumococcal cell wall-degrading virulence factors. J. Biol. Chem. **280:**19948–19957. http://dx.doi.org/10.1074/jbc.M501236200.
16. **Varea J, Saiz JL, López-Zumel C, Monterroso B, Medrano FJ, Arrondo JL, Iloro I, Laynez J, Garcia JL, Menéndez M.** 2000. Do sequence repeats play an equivalent role in the choline-binding module of pneumococcal LytA amidase? J. Biol. Chem. **275:**26842–26855. http://dx.doi.org/10.1074/jbc.M004379200.
17. **De Las Rivas B, García JL, López R, García P.** 2002. Purification and polar localization of pneumococcal LytB, a putative endo-beta-N-acetylglucosaminidase: the chain-dispersing murein hydrolase. J. Bacteriol. **184:**4988–5000. http://dx.doi.org/10.1128/JB.184.18.4988-5000.2002.
18. **Díaz E, García E, Ascaso C, Méndez E, López R, García JL.** 1989. Subcellular localization of the major pneumococcal autolysin: a peculiar mechanism of secretion in Escherichia coli. J. Biol. Chem. **264:**1238–1244.
19. **Schlag M, Biswas R, Krismer B, Kohler T, Zoll S, Yu W, Schwarz H, Peschel A, Götz F.** 2010. Role of staphylococcal wall teichoic acid in targeting the major autolysin Atl. Mol. Microbiol. **75:**864–873. http://dx.doi.org/10.1111/j.1365-2958.2009.07007.x.
20. **Zoll S, Schlag M, Shkumatov AV, Rautenberg M, Svergun DI, Götz F, Stehle T.** 2012. Ligand-binding properties and conformational dynamics of autolysin repeat domains in staphylococcal cell wall recognition. J. Bacteriol. **194:**3789–3802. http://dx.doi.org/10.1128/JB.00331-12.
21. **Fischer W, Behr T, Hartmann R, Peter-Katalinić J, Egge H.** 1993. Teichoic acid and lipoteichoic acid of Streptococcus pneumoniae possess identical chain structures. A reinvestigation of teichoid acid (C polysaccharide). Eur. J. Biochem. **215:**851–857. http://dx.doi.org/10.1111/j.1432-1033.1993.tb18102.x.
22. **Berg KH, Stamsås GA, Straume D, Håvarstein LS.** 2013. Effects of low PBP2b levels on cell morphology and peptidoglycan composition in Streptococcus pneumoniae R6. J. Bacteriol. **195:**4342–4354. http://dx.doi.org/10.1128/JB.00184-13.
23. **Hesek D, Lee M, Morio K, Mobashery S.** 2004. Synthesis of a fragment of bacterial cell wall. J. Org. Chem. **69:**2137–2146. http://dx.doi.org/10.1021/jo035583k.
24. **Hesek D, Suvorov M, Morio K, Lee M, Brown S, Vakulenko SB, Mobashery S.** 2004. Synthetic peptidoglycan substrates for penicillin-binding protein 5 of gram-negative bacteria. J. Org. Chem. **69:**778–784. http://dx.doi.org/10.1021/jo035397e.
25. **Blanchet CE, Zozulya AV, Kikhney AG, Franke D, Konarev PV, Shang WF, Klaering R, Robrahn B, Hermes C, Cipriani F, Svergin DI, Roessle M.** 2012. Instrumental setup for high-throughput small- and wide-angle solution scattering at the X33 beamline of EMBL, Hamburg. J. Appl. Crystallogr. **45:**489–495. http://dx.doi.org/10.1107/S0021889812013490.
26. **Franke D, Kikhney AG, Svergun DI.** 2012. Automated acquisition and analysis of small angle X-ray scattering data. Nucl. Instrum. Methods Phys. Res. A **689:**52–59. http://dx.doi.org/10.1016/j.nima.2012.06.008.
27. **Guinier A.** 1939. La diffraction des rayons X aux très pétits angles: application à l'etude de phénomènes ultramicroscopiques. Ann. Phys. **12:**67.
28. **Svergun DI.** 1992. Determination of the regularization parameter in indirect-transform methods using perceptual criteria. J. Appl. Crystallogr. **25:**495–503. http://dx.doi.org/10.1107/S0021889892001663.
29. **Carrasco-Lopez C, Rojas-Altuve A, et al.** 2011. Crystal structures of bacterial peptidoglycan amidase AmpD and an unprecedented activation mechanism. J. Biol. Chem. **286**(36):31714–31722.
30. **Guan R, Brown PH, et al.** 2006. Crystal structure of human peptidoglycan recognition protein I alpha bound to a muramyl pentapeptide from Gram-positive bacteria. Protein Sci. **15**(5):1199–1206.
31. **Guan R, Roychowdhury A, et al.** 2004. Structural basis for peptidoglycan binding by peptidoglycan recognition proteins. Proc. Natl. Acad. Sci. U. S. A. **101**(49):17168–17173.
32. **Kerff F, Petrella S, et al.** 2010. Specific structural features of the N-acetylmuramoyl-L-alanine amidase AmiD from Escherichia coli and mechanistic implications for enzymes of this family. J. Mol. Biol. **397**(1):249–259.
33. **Korndorfer IP, Danzer J, et al.** 2006. The crystal structure of the bacteriophage PSA endolysin reveals a unique fold responsible for specific recognition of Listeria cell walls. J. Mol. Biol. **364**(4):678–689.
34. **Low LY, Yang C, et al.** 2011. Role of net charge on catalytic domain and influence of cell wall binding domain on bactericidal activity, specificity, and host range of phage lysins. J. Biol. Chem. **286**(39):34391–34403.
35. **Low LY, Yang C, et al.** 2005. Structure and lytic activity of a Bacillus anthracis prophage endolysin. J. Biol. Chem. **280**(42):35433–35439.
36. **Lacks S, Hotchkiss RD.** 1960. A study of the genetic material determining an enzyme in Pneumococcus. Biochim. Biophys. Acta **39:**508–518.